Supramolecular Chemistry

ISSN: (Print) (Online) Journal homepage: https://www.tandfonline.com/loi/gsch20

Synthesis, structural characterization, antibiotics sensing and coordination chemistry of a fluorescent 4-amino-1,8-naphthalimide Tröger's base supramolecular scaffold

June I. Lovitt, Deivasigamani Umadevi, Pandi Raja Lakshmi, Brendan Twamley, Thorfinnur Gunnlaugsson & Sankarasekaran Shanmugaraju

To cite this article: June I. Lovitt, Deivasigamani Umadevi, Pandi Raja Lakshmi, Brendan Twamley, Thorfinnur Gunnlaugsson & Sankarasekaran Shanmugaraju (2020) Synthesis, structural characterization, antibiotics sensing and coordination chemistry of a fluorescent 4-amino-1,8-naphthalimide Tröger's base supramolecular scaffold , Supramolecular Chemistry, 32:12, 620-633, DOI: 10.1080/10610278.2021.1889551

To link to this article: https://doi.org/10.1080/10610278.2021.1889551

SUPRAMOLECULAR CHEMISTRY
2020, VOL. 32, NO. 12, 620–633
https://doi.org/10.1080/10610278.2021.1889551

Taylor & Francis
Taylor & Francis Group

ARTICLE

Synthesis, structural characterization, antibiotics sensing and coordination chemistry of a fluorescent 4-amino-1,8-naphthalimide Tröger's base supramolecular scaffold

June I. Lovitt[a,b], Deivasigamani Umadevi[a], Pandi Raja Lakshmi[c], Brendan Twamley[a], Thorfinnur Gunnlaugsson[a,b,d] and Sankarasekaran Shanmugaraju[c]

[a]School of Chemistry and Trinity Biomedical Sciences Institute, Trinity College Dublin, the University of Dublin, Dublin 2, Ireland; [b]Synthesis and Solid-State Pharmaceutical Centre (SSPC) School of Chemistry, Trinity College Dublin, The University of Dublin, Dublin 2, Ireland; [c]Discipline of Chemistry, Indian Institute of Technology Palakkad, Kerala, India; [d]AMBER (Advanced Materials and Bioengineering Research) Centre, Trinity College Dublin, the University of Dublin, Dublin 2, Ireland

ABSTRACT

The solvothermal synthesis and structural characterization of two new supramolecular coordination polymers featuring a unique V-shaped ligand bis-[*N*-(3-pyridyl)methyl)]-9,18-methano-1,8-naphthalimide-[*b*,*f*][1,5]diazocine (**TBNap**), are reported. The ligand **TBNap** was synthesized as a racemic mixture and the molecular structure was analyzed crystallographically. **TBNap** showed a positive solvatochromism effect which was further supported by DFT calculations illustrating the D-π-A type fluorophore effects within the ligand structures. **TBNap** was further employed as a potential fluorescence probe for the discriminative sensing of structurally assorted antibiotics. A strong fluorescence quenching and preferential binding affinity were realized for nitro-containing antibiotics, i.e., Furazolidone, Nitrofurantoin and Nitrofurazone. The solvothermal reaction of **TBNap** with Cd(OAc)2·2H2O afforded a one-dimensional coordination polymer (TB-CP-1, *poly*-[Cd(**TBNap**)(OAc)2]). Similarly, reaction between **TBNap** and CdCl2.4H2O in DMF-C2H5OH rendered a 4,4′-2D coordination sheet (TB-CP-2, *poly*-[CdCl2(**TBNap**)]·DMF). The extended polymeric structures are further propagated into 3D supramolecular network through multiple face-to-face π-π interaction.

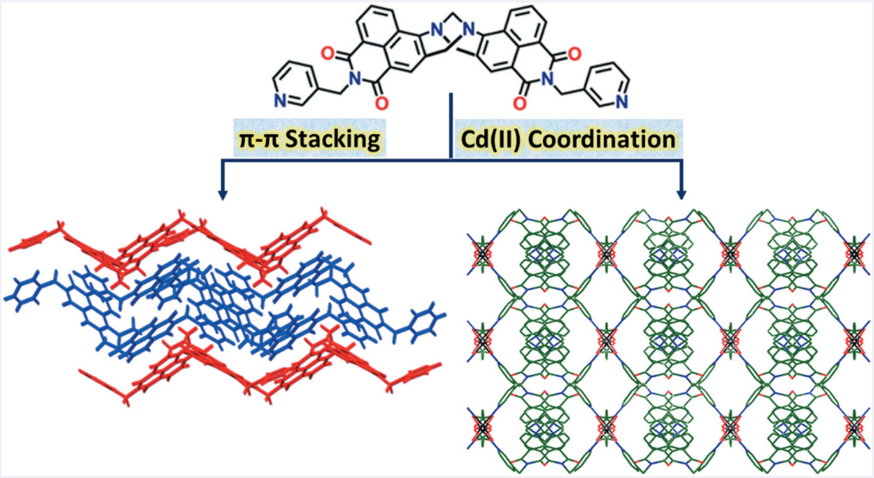

ARTICLE HISTORY
Received 17 December 2020
Accepted 7 February 2021

KEYWORDS
Naphthalimide; tröger's Base; fluorescent sensing; coordination Polymer; solvatochromism

Introduction

The rational design and construction of functional supramolecular coordination polymers (SCPs) have received considerable attention and significant advancement has been made in the past decades, due to their fascinating structural features and diverse applications [1,2]. Supramolecular self-assembly is a powerful synthetic method that provides a facile route to design intricate structures and materials from simple building blocks [3–5]. In general, SCPs are readily formed through self-

CONTACT Thorfinnur Gunnlaugsson gunnlaut@tcd.ie School of Chemistry and Trinity Biomedical Sciences Institute, Trinity College Dublin the University of Dublin, Dublin 2, Ireland; Sankarasekaran Shanmugaraju shanmugam@iitpkd.ac.in Discipline of Chemistry, Indian Institute of Technology Palakkad, Kerala, India.

assembly of a metal ion or metal clusters with multidentate organic/hybrid bridging linkers [6,7]. The functional properties of SCPs including high surface area, strong adsorption affinity, optical and magnetic properties can be systematically tailored for specific applications by the sensible selection of precursors and tuning of the reaction conditions [8–11]. In particular, the luminescent properties of SCPs can be modulated by incorporating stimuli-responsive fluorescent organic linkers such as tetraphenyl ethylene, imidazole, pyrazole, and 4,4′-bipyridine [12–14]. Luminescent SCPs through their selective response to analytes (emission enhancement or quenching) have been utilised in the sensing of toxic organic molecules and ions [15–18]. Amongst the myriad of SCPs, those with accessible nitrogen sites have attracted special attention because of their various application in gas storage, selective adsorption, and sequestration of environmental contaminants [14,19–25].

Antibiotics are well-known medicines widely used for the successful treatment and prevention of various bacterial infections in both humans and animals [26]. Beside their use as antibacterial agents, now antibiotics are considered harmful organic pollutants because of their pernicious effect on the natural environment and living organisms. The extensive use and inappropriate discarding of antibiotics have led to the excessive accumulation of antibiotics in the ecosystem posing serious health problems as well as damage to the environment[27]. For instance, it has been found that the long-term ingestion of antibiotics into human health causes several health-related issues such as hepatotoxicity, allergic reactions, and genetic disorders including cancers [28]. Therefore, the development of suitable chemical sensors for sensitive and selective detection of antibiotics is important for the improvement of human health and removal of environmental pollutions. Recently, fluorescence techniques have become an efficient sensing method for the trace detection of analytes because of their superior sensitivity, portability, and quick response for detection. A wide variety of fluorescence sensors such as luminescent metal-organic frameworks (LMOFs), covalent-organic polymers (COPs), small-molecules, quantum dots, and supramolecular gels are developed and successfully used for the trace detection of electronically assorted antibiotics in both organic and aqueous medium[29]. Among these sensors, small-molecule based fluorescence sensors are attractive because of their facile synthesis, easy purification, and enhanced solution processibility[30].

It has been reported that the introduction of Lewis basic nitrogen open sites in the backbone of permanently porous coordination polymers showed selective gas adsorption and enhanced uptake capacity for CO_2 owing to their basicity and polar C···N interactions [31–34]. However, the construction of SCPs with Lewis basic nitrogen open sites within the ligand skeleton is synthetically challenging due to the significant possibility of competitive binding of metal ions to these sites[12]. The design and use of synthetic constructs for the direct incorporation of non-coordinating open nitrogen-sites into SCPs are rather challenging to achieve [35,36]. Semi-rigid/flexible functionalised pyridyl ligands have been proven to be excellent bridging moieties for building up SCPs because the coordination requirements of the metal ions can be fulfilled through backbone bending of an appropriate twist angle, enabling various conformations to be adopted [37,38]. Here we used a 4-amino-1,8-naphthalimide derived Tröger's base supramolecular scaffold (**TBNap**) to assemble two nitrogen-rich SCPs with Lewis base open sites. **TBNaps** are fascinating chiral scaffolds comprising of a methano-1,5-diazocine ring placing two 1,8-naphthalimide moieties almost at right angles to each other giving rise to a unique V-shaped structure possessing a large internal hydrophobic cavity (Figure 1) [39–45]. Over the past several years, we have been interested in employing **TBNaps** as a bifunctional scaffold to generate various self-assembled structures, soft-materials, and extended polymeric networks for their application within the material and medicinal chemistry fields [46–52]. In this article we present the synthesis, structural characterisation and solvatochromism of **TBNap**, bis-[*N*-(3-pyridyl)methyl)]-9,18-methano -1,8-naphthalimide-[*b*,*f*][1,5]diazocine. Additionally, the antibiotic sensing propensity of **TBNap** is explained in detail. We recently have reported [52] two coordination polymers based on **TBNap** and in continuation, herein we report two new SCPs, *poly*-[Cd(**TBNap**)(OAc)$_2$] (**TB-CP-1**) and *poly*-[CdCl$_2$ (**TBNap**)]·DMF (**TB-CP-2**) generated *via* coordination-driven self-assembly of Cd(II) metal ion and **TBNap**. The present study demonstrates the solvothermal synthesis, structural and thermal characterisation of **TB-CP-1** and **TB-CP-2**.

Results and discussion

Synthesis and Structural Characterisation of TBNap. The ligand **TBNap** was synthesised from the corresponding amino derivative, 4-amino-1,8-naphthalimide (**Nap**) following the procedure reported in our recent literature [52]. The precursor **Nap** was obtained by catalytic hydrogenation of 4-nitro-1,8-naphthalic anhydride with 10%

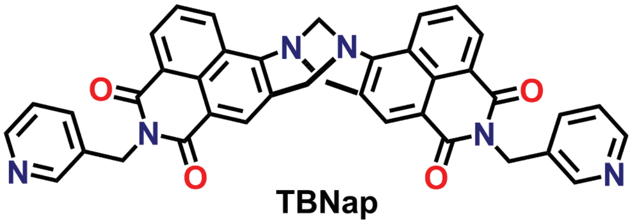

Figure 1. Structure of dipyridyl Tröger's base linker (**TBNap**).

Pd/C at 3 atm of H_2 in dimethylformamide. The **Nap** was then converted into **TBNap**, by using 1.5 equivalent of paraformaldehyde in neat trifluoroacetic acid under an inert atmosphere over 12 hours at room temperature. The resulting reaction mixture was basified (pH > 10) using aq.NH_3, followed by extraction into dichloromethane, which gave the desired dipyridyl-**TBNap** as a racemic mixture in 83% yield after trituration with cold diethyl ether.[‡] The formation of **TBNap** was fully characterised by using various conventional spectroscopic techniques such as FT-IR, multinuclear [^{1}H and ^{13}C] NMR, and HRMS [for details see the Experimental Section and Figures S1-S4 (ESI)]. The [1]H NMR spectrum confirmed the identity of **TBNap** by the well-separated doublet of doublets between 5.17 and 4.67 ppm corresponding to the methylene protons of the Tröger's base cleft (Figure S1, ESI). The high-resolution mass spectrometry (HRMS) analysis of **TBNap** showed one sharp peak at m/z = 643.2069 corresponding to the protonated molecular ion $[M + H]^+$ (Figure S3, ESI)[52].

The molecular structure of **TBNap** was further confirmed by using X-ray diffraction analysis. Suitable single crystals of **TBNap** were obtained by recrystallisation from a hot DMF solution after standing at room temperature for 48 hours. Crystallographic data and refinement parameters are summarised in Table S2 (ESI). The X-ray diffraction analysis of yellow plate crystals, which were isolated by filtration, provided a structural model in the triclinic *P*-1 space group. The diffraction data were modelled as a two-component inversion twin as presented in Figure 2A. The asymmetric unit contained two unique molecules of the ligand each with full chemical occupancy. The structural model clearly shows that the **TBNap** molecule adopts the unique bent to 'V-shaped' conformation, with a mean interplanar angle of 113.921(10)° between the two 1,8-naphthalimide ring systems. The 3-pyridyl substituents attached to the imide nitrogen atom sites face outwards from the cleft, twisted at a mean interplanar angle of 62.394(8)°, no solvent molecules or other guests were located within the lattice. The extended structure of **TBNap** features C-H···π interactions between adjacent parallel moieties as well as C-H···O interactions between 3-pyridyl C-H groups and neighbouring naphthalimide oxygen atoms (C-H···O interaction (2.5125(3) Å, C···O distance 3.0594(4) Å and C-H···O 151.557(3)°). Adjacent 1,8-naphthalimide groups are arranged into a dimer capped by 3-pyridyl moieties through offset face-to-face π-π stacking interactions resulting in the head-to-tail arrangements of the **TBNaps**, as illustrated in Figure 2B.

Solvatochromism and Theoretical Study. The 4-amino-1,8-naphthalimide and its Tröger's base derivatives are found to be strongly coloured and fluorescent owing to the intramolecular charge-transfer (ICT) based excited state, which gives rise to the solvent polarity dependent large excited-state dipole [46–57]. To corroborate the effect of solvent polarity, the absorption, and

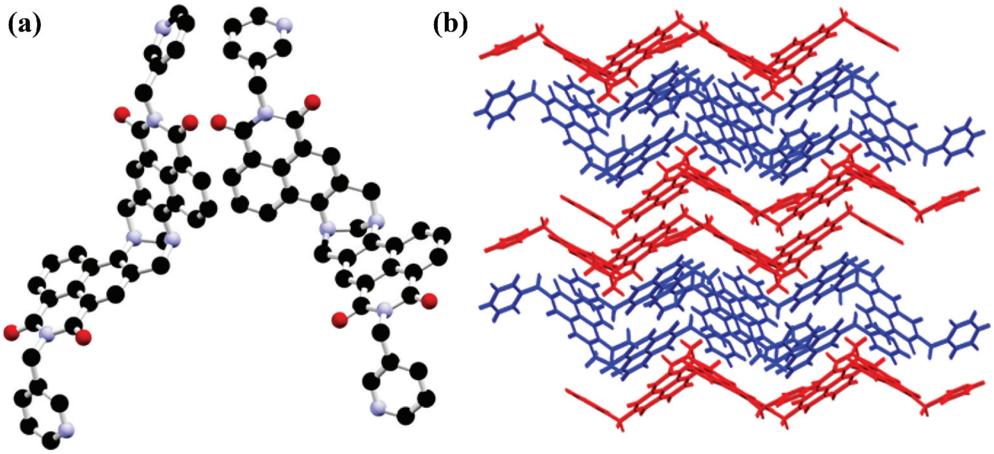

Figure 2. (A) Structure of Ligand **TBNap** as determined by X-ray crystallography. Two unique molecules exist within the unit cell. Hydrogen atoms are omitted for clarity. (B) Intermolecular interactions between adjacent moieties of **TBNap**. Two unique molecules are coloured red and blue, respectively. The orientation illustrates the packing to form a capped dimer with offset face to face π-π stacking interactions between groups.

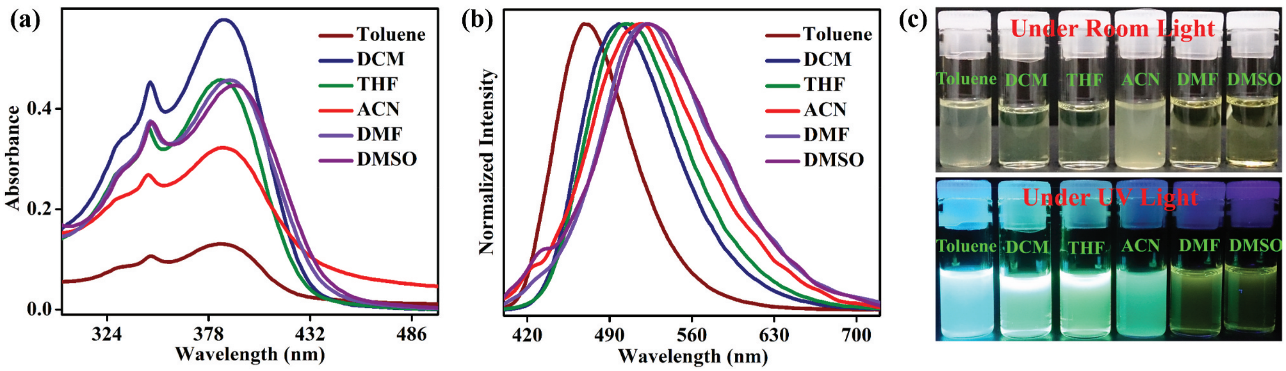

Figure 3. **(A)** UV-visible absorption and **(B)** normalised fluorescence emission spectra of **TBNap** in different polar solvents. **(C)** Corresponding photographs were taken in room light and under UV light.[52].

the fluorescence emission properties of **TBNap** was assessed in different solvents of varying polarity. The corresponding photophysical data are summarised in Table S1 (ESI). **TBNap** was fully soluble in CH_2Cl_2, THF, DMF, and DMSO, but sparingly soluble in toluene and CH_3CN and insoluble in H_2O. The electronic absorption spectra of **TBNap** in both polar and non-polar solvents showed a high-energy band at 345–348 nm which is ascribed to the π-π* transition and a low energy transition at 385–391 nm which is assigned to the ICT transition (Figure 3A). The absorption spectra of **TBNap** showed almost negligible changes in the absorption maxima with increasing polarity of medium and thus the effect of solvent polarity in the ground state was inconsequential. In contrast, the emission spectra of **TBNap** displayed a positive solvatochromism, where the emission maxima corresponding to the ICT transition was significantly red-shifted upon increasing solvent polarity (Figure 3B). This agrees with the nature of the excited state, for example, in the low-polar solvent toluene (P = 2.4) a strong blue-emission band observed, with λ_{max} at 469 nm, while in a polar solvent such as DMSO (P = 7.2) a yellow-green emission was observed with λ_{max} at 524 nm. Notably, a significant increase in Stokes shift from 83 to 133 nm was also observed along with noticeable spectral broadening upon increasing the solvent polarity. These results confirm that the electronically excited state of **TBNap** is more stabilised in highly polar solvents [52,58–62]. As is depicted in Figure 3C, the observed bathochromic shift was also clearly visible to the naked eye; a feature we have previously capitalised on for the discriminative detection of volatile organic pollutants[63].

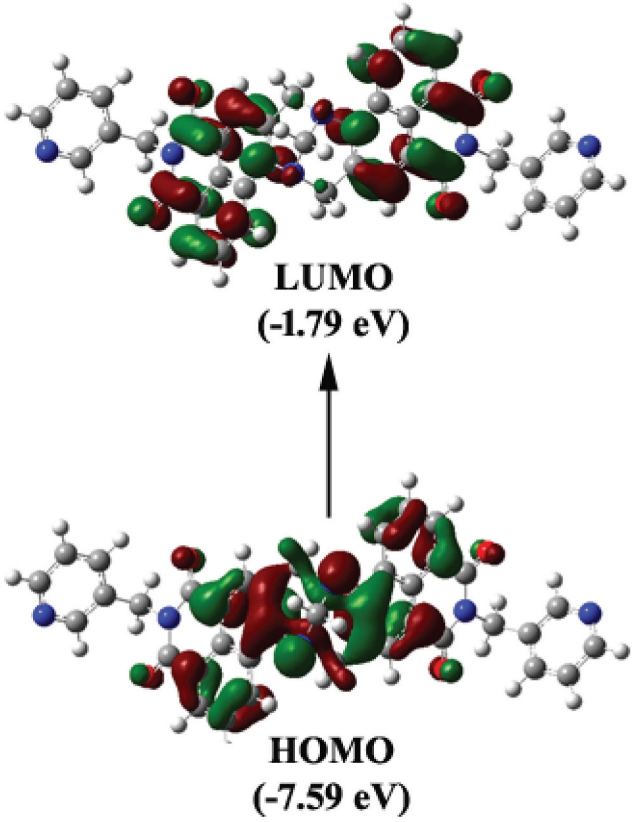

Figure 4. Frontier molecular orbitals (HOMO and LUMO) of **TBNap.**

To further validate the experimentally observed ICT transition, we performed theoretical calculations using the density functional theory (DFT) approach on **TBNap** structure to obtain the energy minimised structure and frontier molecular orbital diagrams. The DFT calculations were carried out at the M062X/6-31 G(d,p) [64] level using the Gaussian 09 program[65]. It revealed that the highest occupied molecular orbital (HOMO) (−7.59 eV) was primarily distributed on the Tröger's base (TB) unit itself (acting as a donor), while the lowest unoccupied molecular orbital (LUMO) (−1.79 eV) was more localised on the **Nap** unit (acting as an acceptor), as demonstrated in Figure 4. These results show that **TBNap** is a typical D-π-A type fluorophore and hence, strongly supports the 'push-pull' based ICT transition from the electron-

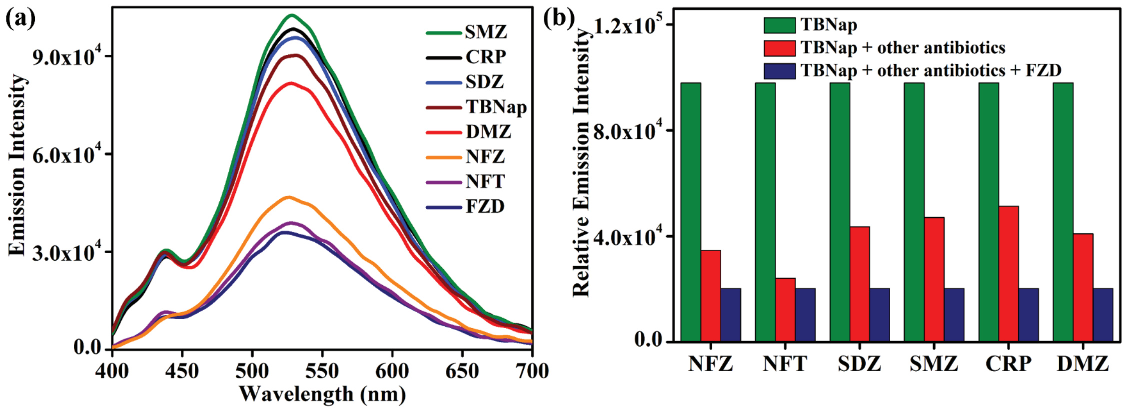

Figure 5. (A) The changes in the fluorescence emission spectra of **TBNap** upon the addition of different antibiotics in DMSO medium; (B) Competitive binding affinity of **TBNap** towards different antibiotics in the absence (red) and the presence (blue) of FZD antibiotic.

donating TB unit to the electron-accepting imide moiety [53–62]. Moreover, the structural features of the optimised geometry of **TBNap** concur well with the structure obtained from the X-ray diffraction analysis above.

Fluorescence Sensing of Antibiotics.

Inspired by its excellent photophysical characteristics, herein we have used **TBNap** as a small-molecular fluorescence probe for the detection of antibiotics. The following antibiotics were chosen for the fluorescence sensing studies: Nitrofurantoin (NFT), Nitrofurazone (NFZ), Sulphadiazine (SDZ), Sulphamethazine (SMZ), Chloramphenicol (CRP), Furazolidone (FZD), Dimetridazole (DMZ). To explore the selectivity of **TBNap** for antibiotics detection, we first measured the emission intensity of **TBNap** in the presence of different antibiotics listed above in the DMSO medium. As shown in Figure 5A, **TBNap** showed discriminative fluorescence sensing responses for different antibiotics. The nitro-containing antibiotics such as FZD, NFT, and NFZ exhibited the highest fluorescence quenching due to their electron-deficient nature enhanced by the electron-withdrawing NO_2 groups. In sharp contrast, electron-rich antibiotics such as SMZ, CRP, and SDZ displayed little enhancement in emission intensity. These studies confirmed the high selectivity of **TBNap** towards nitro-containing antibiotics. To further corroborate the high selectivity of **TBNap**, competitive fluorescence studies using FZD as a representative example were performed in the presence of other interfering antibiotics. As illustrated in Figure 5B, where the initial emission intensity (red bar) of **TBNap** was moderately quenched (green bar) upon the addition of other interfering antibiotics. However, the subsequent mixing of FZD elicited a significant fluorescence quenching (blue bar) further confirming the preferential binding affinity of **TBNap** for nitro-containing antibiotics.

To further determine the sensing propensity of **TBNaps** for antibiotic detections, a fluorescence titration experiment was performed using FZD. As shown in Figure 6, the initial emission intensity of **TBNap** at λ_{max} = 524 nm was quenched significantly upon the addition of FZD in increasing concentrations. No other

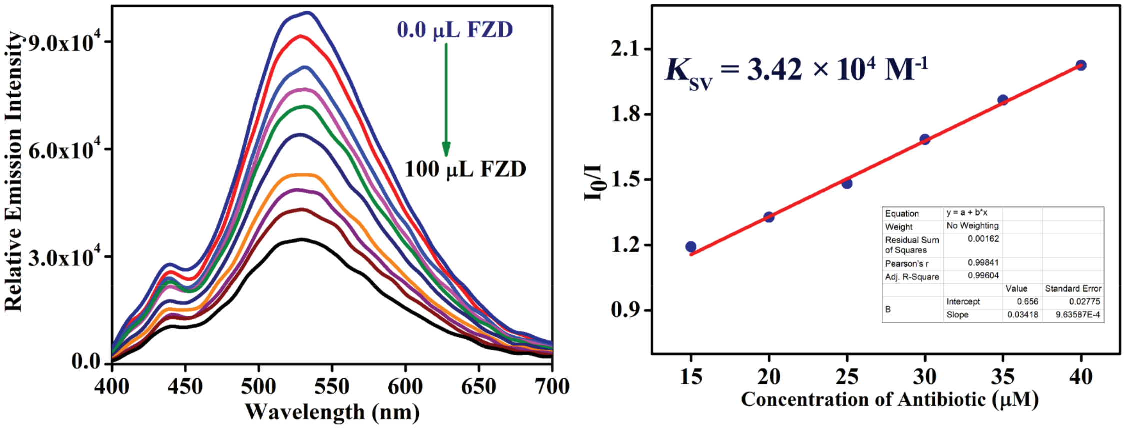

Figure 6. The extend of fluorescence quenching (left) of **TBNap** upon the addition of increasing concentration of FZD antibiotics and its corresponding Stern-Volmer plot (right).

remarkable spectral changes, such as a shift in λ_{max}, are observed. The change in emission intensity of **TBNap** was analysed by fitting the titration data to the well-known Stern-Volmer equation:

$I_0/I = 1 + K_{SV}[Q]$

where, I_0 and I are the fluorescence intensity before and after the addition of analyte, respectively, [Q] is the molar concentration of analytes, and K_{SV} is the Stern-Volmer binding constant. From the fluorescence titration profile, a linear Stern-Volmer plot (Figure 6) was obtained and binding constant K_{SV} was determined as $3.42 \times 10^4\ M^{-1}$, which is comparable to other reported fluorescence sensors for FZD detection [66] and the high K_{SV} value demonstrates preferential binding affinity of **TBNap** for antibiotics. The significant spectral overlap of the absorption spectrum of analyte FZD with emission spectra of sensor **TBNap** supports that an excited state energy transfer mechanism operates between **TBNap** and FZD (Figure S5, ESI). Therefore, the observed substantial fluorescence quenching of **TBNap** in presence of FZD is attributed to the efficient charge-transfer (CT) complex formation between electron-rich **TBNap** and electron-deficient FZD.

To investigate the fluorescence quenching response time to sense FZD by **TBNap**, we then performed a time-dependent fluorescence titration study. The emission intensity of **TBNap** was monitored at different time-intervals and quenching efficiency was plotted against exposure time as shown in Figure S6 (ESI), which demonstrates a fast fluorescence sensing response for FZD detection. For instance, approximately 50% of quenching efficiency was observed within 60 s of exposure time and thus, **TBNap** can be considered a quick sensor to detect antibiotics. To determine the sensitivity of **TBNap**, a similar fluorescence titration was performed taking FZD at an extremely low concentration of FZD. The limit of detection (LOD) was estimated by using the following equation:

Limit of detection = $3\sigma/K$

Where σ is the standard deviation of the initial emission intensity of **TBNap** and K is the slope of the linear calibration curve. As depicted in Figure S7 (ESI), a plot of change in emission intensity as a function of FZD concentration gave a linear curve with slope $K = 13.92 \times 10^6$. The quantitative analysis of fluorescence titration data fitting into the above equation revealed that **TBNap** can indicate the presence of FZD as low as 6.82 ppm. These studies demonstrate the potential of **TBNap** for the fast and sensitive detection of antibiotics in solution.

Synthesis and structure of the *poly*-[Cd(TBNap)(OAc)$_2$] TB-CP-1. Having synthesised and structurally characterised, we subsequently explored the coordination chemistry of **TBNap** in the synthesis of two new supramolecular coordination polymers **TB-CP-1** and **TB-CP-2**. These coordination polymers were each formed from the solvothermal reaction of **TBNap** and the appropriate Cd(II) metal salt in a 1:2 molar ratio in DMF or DMF-C_2H_5OH solvent mixtures as specified below. The solid-state structure of these polymers was analysed through single-crystal X-ray diffraction. The chemical composition and purity of the complexes were determined using elemental analysis and powder X-ray diffraction analysis, respectively. The reaction of **TBNap** and $Cd(OAc)_2{\cdot}2H_2O{\cdot}$ in a 1:2 stoichiometry in DMF afforded X-ray diffraction quality yellow block crystals of **TB-CP-1** after heating at 100°C for 48 h. Analysis by single-crystal X-ray diffraction provided a structural model in the monoclinic *P*2/c space group, revealing a polymeric structure with the formula *poly*-[Cd(**TBNap**)(OAc)$_2$] as shown in Figure 7A. The asymmetric unit of *poly*-[Cd(**TBNap**)(OAc)$_2$] contains half of one molecule of **TBNap** and a Cd(II) ion exhibiting slightly distorted octahedral six-coordinate geometry; the coordination sphere being further occupied by two equivalent pyridyl nitrogen atoms and two bidentate acetato ligands. The nitrogen and oxygen atoms coordinate at Cd-N and Cd-O distances 2.32921(15) Å and 2.30594(18) Å for N1 and O2, respectively. All Cd(II) ions are in equivalent environments. The compound exhibits a densely packed structure and there are no solvent molecules or other guest molecules located within the lattice (Figure 7B). The **TBNap** molecule within *poly*-[Cd(**TBNap**)(OAc)$_2$] adopts the expected cleft conformation between the two naphthalimide rings (112.983(6)°). The bulk structure of the complex illustrates face-to-face π-π interactions between adjacent **Nap** groups at a mean interplanar angle of 2.648° and minimum interatomic distance of 3.8776(3) Å for C11···C11. There are also C-H···O interactions both between the acetate ligands and nearest **TBNap** C-H group which exhibit a relatively short C···O distance of 2.6684(14) Å and a C-H···O angle of 148° as well as between the 3-picolyl group and the adjacent **TBNap** unit; the C-H···O interaction has a distance of 2.4220 (13) Å and angle 172.50(12)°. There are also weak C-H···π interactions between adjacent **TBNap** units with 2.8211(15) Å and angle 149.5°. Thermogravimetric analysis of an air-dried sample of **TB-CP-1** corresponded with no solvent being present in the unit cell of the crystal as the sample remained stable with no mass loss occurring until 300°C. Above 300°C, decomposition of the remaining organic proportion of the framework is observed (Figure S8, ESI). The X-ray powder diffraction patterns of complex **TB-CP-1** convincingly match with the simulated powder pattern at 100 K of the crystal indicating that the crystallinity of the complex was

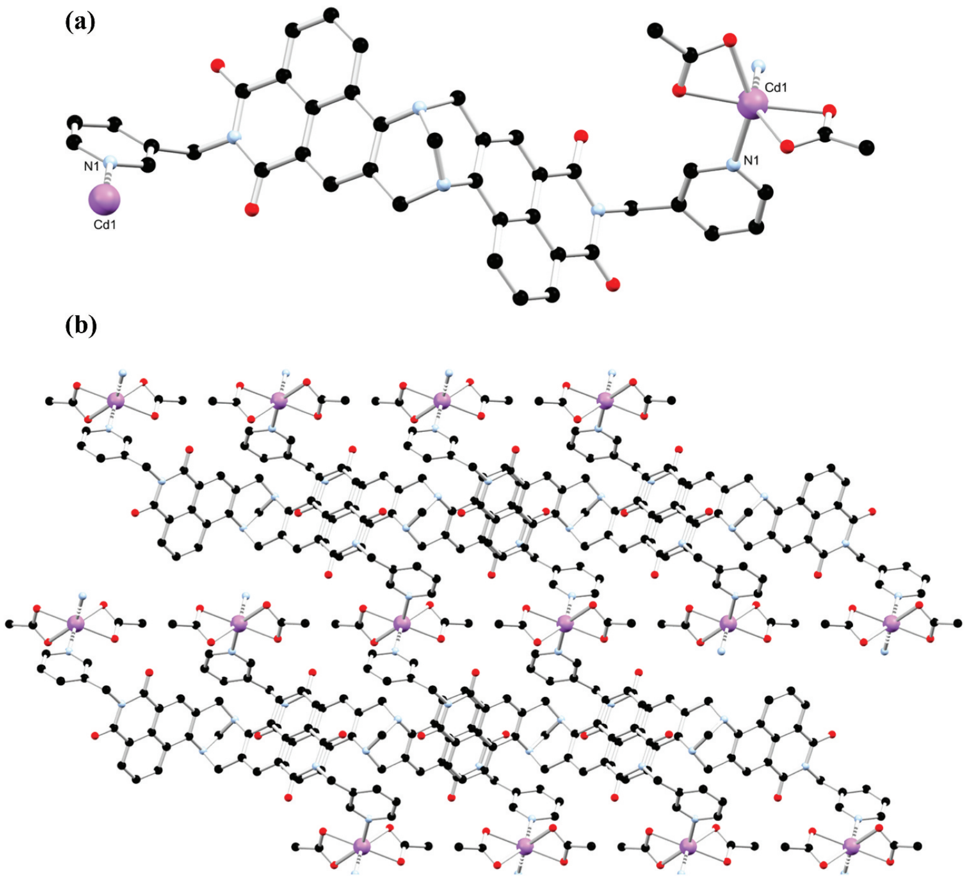

Figure 7. **(A)** Structure of complex **TB-CP-1** with labelling scheme for unique heteroatoms. **(B)** Intermolecular interactions in the structure of **TB-CP-1** showing face to face π-π stacking interactions between adjacent complexes. Hydrogen atoms are omitted for clarity.

retained in the bulk structure (Figure S9, ESI). Additionally, Le Bail refinement of the powder diffraction data was undertaken, indicating a good agreement between the bulk room temperature data and single-crystal calculated data, a good degree of phase purity (Figure S10, ESI).

Synthesis and Structure of *poly*-[CdCl$_2$(TBNap)]·DMF (TB-CP-2): The reaction between **TBNap** and CdCl$_2$•4H$_2$O in a 1:2 stoichiometry ratio in DMF-EtOH (in 2:1 volume ratio) solutions afforded the diffraction quality yellow block crystals of **TB-CP-2** after heating the solution at 100°C for 24 hours. The crystals were isolated by filtration after washing with fresh DMF. Analysis by single-crystal X-ray diffraction provided a structural model in the monoclinic $P2_1/c$ space group, revealing a polymeric structure with the formula *poly*-[CdCl$_2$(**TBNap**)]·DMF as shown in Figure 8A. The asymmetric unit contains one molecule of **TBNap** and a Cd(II) ion exhibiting octahedral coordination geometry. The other sites in the coordination sphere are occupied by two sets of two equivalent equatorial pyridyl nitrogen atoms and two axial chlorido ligands. The two nitrogen atoms coordinate at Cd-N distances 2.44700(8) Å and 2.40086(6) Å for N1 and N6, respectively. The **TBNap** molecule adopts the expected cleft conformation between the two naphthalimide rings, with a mean inter-planar angle between the naphthalene fragments of 112.4373(16)°. There are also three chemically equivalent partially occupied DMF solvent molecules within the unit cell. The DMF molecules were disordered and the most realistically modelled as chemical occupancy of 0.25 and 0.5 each. The solvent molecules in the extended structure align along the *c* axis perpendicular to the 2D sheet. The extended structure, as illustrated in Figure 8B, is also a 4,4′- two-dimensional coordination polymer containing offset face-to-face π-π interactions between adjacent **Naps** groups at a mean interplanar angle of 4.165° with the minimum interatomic distance of 3.77517(12) Å for C13···C13 as illustrated in Figure 8B. There are also anion···π interactions between the naphthalimide groups and chlorido ligands (π-H···Cl distance 2.75668(9) Å) as well as weak intermolecular interactions between the complex and solvent molecules. Thermogravimetric analysis of an air-dried sample **TB-**

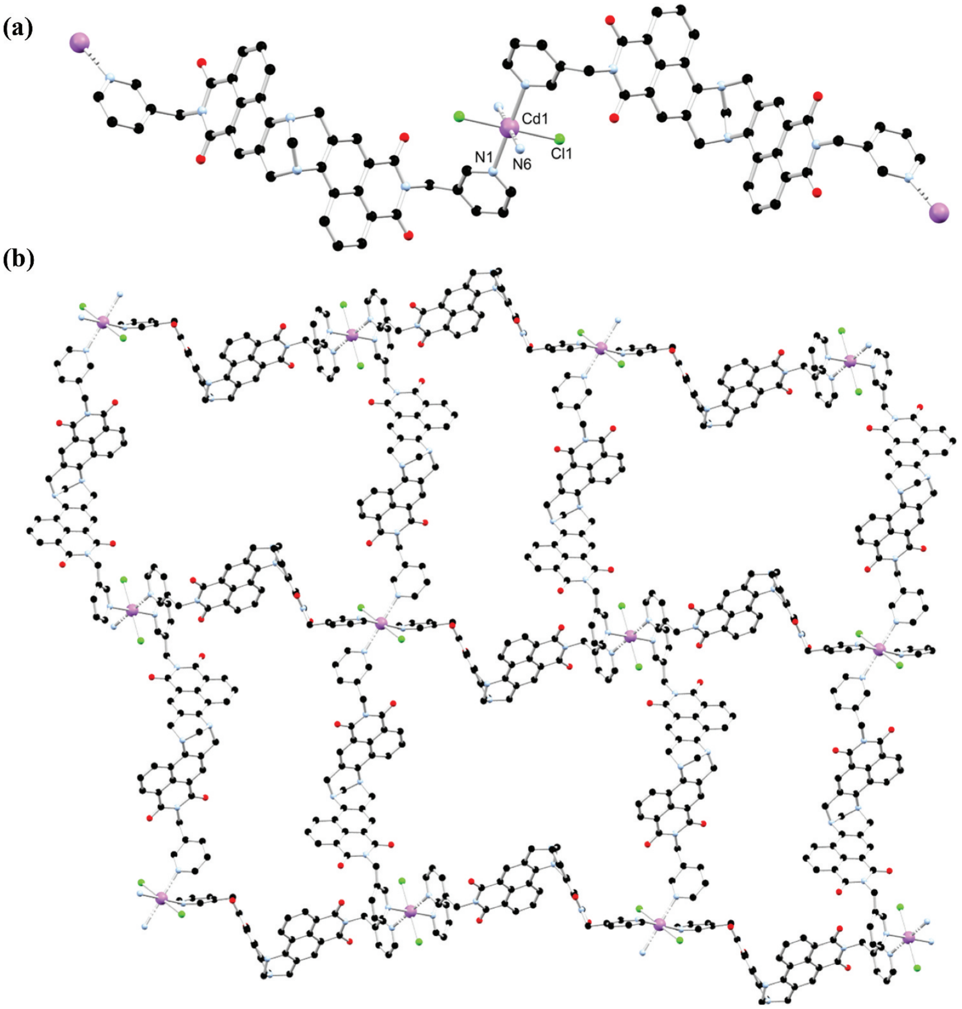

Figure 8. **(A)** Structure of complex **TB-CP-2** with labelling scheme for unique heteroatoms. **(B)** Extended structure in the structure of **TB-CP-2** illustrating the formation of a 4,4′-2D coordination polymer. Hydrogen atoms and partially occupied solvent molecules are omitted for clarity.

CP-2 showed an initial weight loss of 8% occurring in the range 30–180°C, this corresponds to the evaporation of 1 DMF molecule per unit cell. There is a more gradual loss of a further 4% below 380°C, presumably representing a mixture of mobile solvent molecules trapped within the freshly isolated framework which are lost on extended standing in the air. Above 300°C, decomposition of the remaining organic proportion of the framework was observed (Figure S11, ESI). The experimentally observed powder diffraction pattern of the complex **TB-CP-2** matches well with the simulated pattern of the crystal at 100 K confirming that the phase purity is retained in the bulk compound (Figure S12, ESI). Additionally, Le Bail refinement was carried out on the powder diffraction indicating a good agreement between the structural and powder data and a good degree of phase purity (Figure S13, ESI).

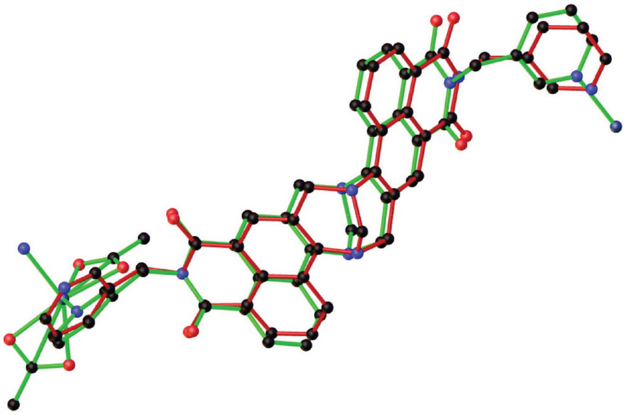

Figure 9. Overlaid structures of **TBNap** and **TB-CP-1** illustrating the difference in the dimensionality of the discrete ligand structure and the coordination polymer. Hydrogens and partially occupied solvents are omitted for clarity.

Structural correlation

The structural arrangements of the two newly synthesised polymeric complexes **TB-CP-1** and **TB-CP-2** presented herein differ from that of the discrete **TBNap** ligand structure. The complex *poly*-[Cd(**TBNap**)(OAc)$_2$] forms a one-dimensional coordination polymer whereas *poly*-[CdCl$_2$(**TBNap**)]·DMF forms a two dimensional 4,4′ sheet. Furthermore, in both the complexes, upon the coordination of pyridyl nitrogen to the Cd(II) metal ion, there is a significant twisting component in the folding of the equivalent pyridyl groups compared to the **TBNap** ligand structure. In **TBNap**, the plane fold angle is 61.090(8)° and twist angle is 15.646(6)°, whereas in *poly*-[CdCl$_2$(**TBNap**)]·DMF the plane fold angle is 72.286(2)° and plane twist angle is 30.787(4)°; in *poly*-[Cd(**TBNap**)(OAc)$_2$] the plane fold angle is 8.146(5)° and twist angle is 125.380(8)°. These distinct structural differences are clearly illustrated in overlaid structures given in Figure 9 and Figure S14 (ESI). Moreover, there are a few meaningful conclusions that can be drawn between comparing these structures with those we have previously reported of **TBNap** with CoCl$_2$ and Cd(NO$_3$)$_2$•4H$_2$O[52]. The solvothermal reaction of **TBNap** and CoCl$_2$ in DMF yielded a one-dimensional extended polymeric structure in which the ligand **TBNap** adopts an expected cleft shape confirmation with a mean inter-planar angle of 81.1° between the naphthalene moieties. The two pyridyl groups of **TBNap** coordinating to Co(II) are twisted inwards towards the cleft and this endowed a zig-zag nature to the polymeric network. Similarly, the reaction of **TBNap** and Cd(NO$_3$)$_2$•4H$_2$O resulted in a one-dimensional polymeric structure consisting of two coaxial zig-zag chains with structurally unique **TBNap** in a more compact cleft conformation. These studies demonstrate that by judicious selection of reacting components and tuning the reaction conditions, several structurally unique supramolecular coordination polymers with interesting functional properties can be generated. We are in the process of investigating these possibilities further.

Conclusions

In summary, we have synthesised two new Cd(II) supramolecular coordination polymers *poly*-[Cd(**TBNap**)(OAc)$_2$] (**TB-CP-1**) and *poly*-[CdCl$_2$(**TBNap**)]·DMF (**TB-CP-2**) from a close to 'V-shaped' fluorescent naphthalimide derived Tröger's base ligand and structurally characterised by using X-ray diffraction analysis. The solid-state structural analysis of the ligand **TBNap** showed that the structure had a mean interplanar angle of 113.921(10)° between the two **Nap** ring systems, which is a somewhat larger angle than we have seen for some other **TBNap** structures, the solution studies demonstrated that **TBNap** displayed a positive solvatochromism, due to the 'push-pull' based ICT transition, in different solvents with varying polarity.‡ The highly emissive **TBNap** was used as a promising fluorescence probe for antibiotic sensing in solution. The fluorescence titration studies demonstrated the preferential and strong binding affinity of **TBNap** towards nitro-containing antibiotics and detect antibiotics at ppm-level. The observed strong fluorescence quenching is ascribed to the excited energy transfer from **TBNap** to antibiotics. The coordination polymers both **TB-CP-1** and **TB-CP-2** were not realised for antibiotics sensing owing to their poor stability in solution and they were found to decompose in the DMSO solution. The coordination properties of **TBNap** were analysed in the solid-state. The crystallographic analysis revealed that **TB-CP-1** is a 1D coordination polymer exhibiting a densely packed extended structure with no solvent or guest molecules located within the crystal lattice. All Cd(II) ions are in an equivalent environment exhibiting distorted octahedral geometry occupied by two equivalent pyridyl nitrogen atoms and two bidentate acetato ligands. The structural analysis unveiled that **TB-CP-2** is a 4,4′-2D coordination polymer network containing three partially occupied DMF solvent molecules within the lattice. The octahedral Cd(II) coordination geometry is occupied by two sets of two equivalent equatorial pyridyl nitrogen atoms and two axial chlorido ligands. In each case, ligand **TBNap** adopts the expected cleft conformation between the two naphthalimide rings and substantial face-to-face π-π interactions between the adjacent chains leading to the structurally interesting supramolecular coordination networks. These results are of major importance in demonstrating the versatility of **TBNap** in fluorescence sensing and constructing coordination polymers with nitrogen-rich open sites for application in energy and environmental-related areas, and such investigations are currently underway in our laboratories.

Experimental section

Materials and General Methods. All reagents, solvents, and starting materials were purchased from various commercial sources, were of reagent grade, and were used as received. Solvents used were HPLC grade unless otherwise stated. 4-Nitro-1,8-naphthalic anhydride, 3-picolylamine, palladium on carbon (10 wt% loading), paraformaldehyde, trifluoroacetic acid (TFA), antibiotics, and all-metal salts used to make polymers were purchased from Sigma-Aldrich and used as received.

Deuterated solvent $(CD_3)_2SO$ used for NMR analyses of ligand were purchased from Sigma-Aldrich or Apollo Scientific. *N*-[(3-pyridyl)methyl]-4-nitro-1,8-naphthalimide and **Nap** precursors were synthesised following the procedure reported in the literature [52,67].

The melting point was determined using an Electrochemical IA9000 digital melting point apparatus in an unsealed capillary tube.

The elemental analysis for C, H, and N was performed on an Exeter analytical CE-450 elemental analyser.

FT-IR spectra were recorded in the range 4000–550 cm^{-1} on a Perkin-Elmer spectrometer equipped with a universal ATR sampling accessory.

All NMR spectra were recorded on a Bruker-DPX-Avance spectrometer operating at 600 MHz for [1]H NMR and 150 MHz for [13]C NMR in the commercially available deuterated solvent. Chemical shifts are reported in parts-per-million (ppm) relative to the internal solvent $(CD_3)_2SO = 2.5$ ppm signal. All NMR data were processed with Bruker Win-NMR 5.0, Topspin, and MestReNova software. Multiplicities were abbreviated as follows: singlet (s), doublet (d), doublet of doublet (dd), triplet (t), multiplet (m).

APCI-ESI mass spectra were acquired on a Bruker microTOF-Q III spectrometer interfaced with a Dionex UltiMate 3000 LC or direct insertion probe. The instrument was operated in the positive or negative mode as required. Agilent tuning mix APCI-TOF was used to calibrate the system. The *m/z* values were recorded over a range of 100–1600. MicroTof control and HyStar software were used to carry out the analysis. HPLC-grade CH_3CN or CH_3OH or DMSO were used as carrier solvents.

Thermogravimetric analysis (TGA) of the complexes was performed on an analyser equipped with an ultra-micro balance with a sensitivity of 0.1 µg. The temperature range was from 25°C to 800°C with a scan rate of 10°C/min under N_2 purge.

X-ray powder diffraction patterns were collected using a Bruker D2 Phaser instrument with Cu Kα radiation ($\lambda = 1.5418$ Å). Samples were ground and mounted on silicon sample holders, and data were collected in the 2θ range 5 – 55° at room temperature. The patterns were compared with those simulated from the single-crystal data collected at 100 K.

UV-visible absorption spectra were recorded in 1 cm quartz cuvettes (Hellma) either on a Varian Cary 50 spectrometer or recorded using a Thermo Scientific evolution 201 spectrometers. Baseline correction was applied for all spectra.

Emission spectra were recorded either on a Varian Cary Eclipse Fluorimeter or recorded using the Perkin Elmer-6500 Fluorimeter. The temperature was kept constant throughout the measurements at 298 K by using a thermostated unit block.

Synthetic procedure

Bis-[*N*-(3-pyridyl)methyl)]-9,18-methano-1,8-naphthalimide-[*b,f*][1,5]diazocine (TBNap)[52]. Compound **Nap** (200 mg, 0.66 mmol, 1 equiv.) and paraformaldehyde (30 mg, 0.99 mmol, 1.5 equiv.) were flushed with argon. Trifluoroacetic acid (4 mL) was added at 0°C and the solution was stirred at room temperature for 12 h under an inert atmosphere. The reaction mixture was then added dropwise to aqueous ammonium hydroxide (100 mL) at 0°C until a pH > 10 was achieved. Dichloromethane (2 × 200 mL) was added, and the organic layer was extracted and washed with saturated $NaHCO_3$ (2 × 100 mL), brine (2 × 100 mL) and H_2O (2 × 100 mL). The solution was dried over $MgSO_4$ and the solvents were removed under reduced pressure to isolate compound **TBNap** (186 mg, 0.27 mmol, 83%) as a bright yellow solid after trituration with cold-diethyl ether. Anal. Calcd (%) for $C_{39}H_{26}N_6O_4 \cdot 0.4CH_2Cl_2$: C, 69.94; H, 3.99; N, 12.42: Found C, 70.21; H, 3.91; N, 12.53. Melting point 283–285°C (decomp.). HRMS (APCI) *m/z*: calcd for $C_{39}H_{27}N_6O_4$ $[M + H^+]$ 643.2094, found 643.2069; [1]H NMR (600 MHz, $(CD_3)_2SO$) δ 8.75–8.73 (2 H, d, *J* = 8.9 Hz, Ar-H), 8.53 (2 H, s, Pyridyl-H), 8.49–8.48 (2 H, d, *J* = 7.3 Hz, Ar-H), 8.40–8.39 (2 H, d, *J* = 6.2 Hz, Pyridyl-H), 8.13 (2 H, s, Ar-H), 8.00–7.93 (2 H, m, Ar-H), 7.64–7.62 (2 H, d, *J* = 8.0 Hz, Pyridyl-H), 7.26–7.23 (2 H, dd, *J* = 7.9, 4.8 Hz, Pyridyl-H), 5.17 (4 H, s, Pyridyl-CH_2), 5.18–5.15 (2 H, d, *J* = 17.4 Hz, NCH_2), 4.72 (2 H, s, NCH_2), 4.68–4.65 (2 H, d, *J* = 17.4 Hz, NCH_2); [13]C NMR (150 MHz, $(CD_3)_2SO$) δ 163.97, 163.39, 149.82, 149.53, 148.73, 135.65, 133.45, 131.48, 130.97, 129.87, 128.05, 127.68, 127.22, 126.71, 123.93, 122.76, 117.94, 66.52, 57.26, 4100; FT-IR υ_{max} (ATR, cm^{-}[1]) 3038, 2156, 1971, 1702, 1654, 1624, 1594, 1581, 1517, 1478, 1460, 1428, 1405, 1378, 1335, 1319, 1231, 1180, 1168, 1120, 1098, 1027, 975, 934, 869, 828, 786, 761, 732, 711, 674, 630, 613,586.

***poly*-[Cd(TBNap)(OAc)$_2$] (TB-CP-1)**. Compound **TBNap** (20 mg, 31.1 µmol) and cadmium(II) acetate dihydrate (16.6 mg, 62.2 µmol) were combined in 3 mL of DMF. The reaction mixture was briefly sonicated, sealed in a Teflon-capped vial and heated at 100°C for 48 h. Yellow crystals were isolated by filtration, washed with fresh DMF (2 × 2 mL) and dried in air. Yield: 12 mg (60%). m.p. > 300°C. Anal. Calcd (%) for $C_{43}H_{32}N_6O_8Cd$: C, 59.15; H, 3.69; N, 9.62: Found C, 57.66; H, 3.88; N, 9.38. FT-IR υ_{max} (ATR, cm^{-}[1]) 2982, 1696, 1657, 1619, 1596, 1570, 1546, 1510, 1482, 1458, 1421, 1401, 1376, 1352, 1333, 1321, 1297, 1254, 1234, 1196, 1166, 1126, 1086, 1050, 1030, 1010, 959, 933, 911, 847, 836, 806,785, 756, 708, 676, 663, 645, 622, 581, 572, 554.

***poly*-[CdCl$_2$(TBNap)]·DMF (TB-CP-2)**. Compound **TBNap** (20 mg, 31.1 µmol) and cadmium(II) chloride (11.4 mg, 62.2 µmol) were combined in a mixture of DMF-EtOH (3 mL in 2:1 volume ratio). The mixture was briefly sonicated, sealed in a Teflon-capped vial, and heated at 100°C for 24 h. Yellow crystals were isolated by filtration, washed with fresh DMF (2 × 2 mL) and dried in air. Yield: 8.5 mg (43%). m.p. > 300°C. Anal. Calcd (%) for $C_{39}H_{26}Cl_2N_6O_4Cd$·DMF: C, 52.16; H, 3.82; N, 9.36: Found C, 53.94; H, 4.14; N, 9.09. FT-IR υ_{max} (ATR, cm^{-}[1]) 2978, 1695, 1650, 1619, 1595, 1569, 1510, 1479, 1458, 1434, 1403, 1373, 1333, 1318, 1301, 1256, 1232, 1169, 1152, 1129, 1105, 1089, 1050, 1023, 1010, 961, 912, 870, 835, 784, 756, 705, 661, 641, 621, 581.

Crystallography

Structural and refinement parameters are presented in Table S2. All diffraction data were measured using a Bruker APEX-II Duo dual-source instrument using graphite-monochromated Mo Kα (λ = 0.71073 Å) as specified. Datasets were collected using ω and φ scans with the samples immersed in NVH immersion oil and maintained at a constant temperature of 100 K using a Cobra cryostream. The data were reduced and processed using the Bruker APEX-3 suite of programs [68] Multi-scan absorption corrections were applied using SADABS[69]. The diffraction data were solved using SHELXT and refined by full-matrix least-squares procedures using SHELXL-2015 within the OLEX-2 GUI [70,71]. All non-hydrogen atoms were refined with anisotropic displacement parameters. All carbon-bound hydrogen atoms were placed in calculated positions and refined with a riding model, with isotropic displacement parameters equal to either 1.2 or 1.5 times the isotropic equivalent of their carrier atoms[72]. Crystals of ligand **TBNap** were processed as a single component, the data was processed with PLATON TwinRotMot[72]. The final refinement was carried out on the merged HKLF 5 file, twin law HKLF 5 BASF [0.243(4)]. The R_{int} value for the individual domain was 6.87. Crystals of *poly*-[Cd(**TBNap**(OAc)$_2$] (**TB-CP-1**) were twinned following the twin law HKLF 5 BASF [0.1494(7)]. The data was processed with TWINABS and the final refinement was carried out on, the merged HKLF 5 files[73]. The R_{int} value for the individual domain was 0.0283. The data was rotated from the first domain by 179.2 degrees about reciprocal axis −0.157 1.000 − 0.016 and real axis −0.079 1.000 − 0.013. The Twin law used to convert hkl from first to this domain (SHELXL TWIN matrix): −0.978 − 0.312 − 0.006 − 0.155 0.975 − 0.026 0.024 − 0.028 − 0.997. Crystals of *poly*-[CdCl$_2$(**TBNap**)]·DMF (**TB-CP-2**) provided good quality diffraction data and the model was refined to convergence with only minimal restraints, mostly involving the partially occupied solvent molecules. Particular refinement strategies for each structure, including the specific use of restraints, are provided in the combined crystallographic information files. CCDC 1864799 – 1864801.

Associated content

Supporting Information.

Spectroscopic [^{1}H, 13C NMR, FTIR, and APCI-MS] characterisation, TGA, powder diffraction, antibiotics sensing, and crystallographic refinement data are available.

Accession codes

CCDC 1,864,799 (**TBNap**), 1864800 (**TB-CP-1**) and 1864801 (**TB-CP-2**) contains the supplementary crystallographic data for this paper.

Foot note

‡While in the current study we used **TBNap** in its racemic form, we have previously demonstrated that such structures can be resolved[49]. While not reported herein [53–57], the solvent effect for the **Nap** itself is generally larger than seen for the **TBNaps** structures as the lone pair of the nitrogen is more delocalised with the ring structures. This can also be seen in the ground and the excited states, as λ_{max} occurs at longer wavelengths.

Notes

Any additional relevant notes should be placed here.

Acknowledgments

The authors gratefully acknowledge the Science Foundation Ireland (SFI PI Award 13/IA/1865, the SFI Centre AMBER (for Research Centres Phase 2 12/RC/2278_P2) and the SFI Centre SSPC (for Research Centres Phase 2 12/RC/2275_P2) to TG), and Science and Engineering Research Board (EMEQ Award EEQ/2018/000799 to SS) for the financial support. RP and SS are thankful to the discipline of Chemistry and CIF-CMFF, IIT Palakkad for spectroscopic analysis. We thank Drs J. E. O'Brien, M. Reuther, and G. Hessman for their help with NMR and HRMS.

Disclosure statement

No potential conflict of interest was reported by the authors.

Funding

This work was supported by the Science Foundation Ireland [SFI PI Award 13/IA/1865; the SFI Centre Amber (for research Centres Phase 2 12/RC/2278_P2) and the SFI Centre SSPC (for Research Centres Phase 2 12/RC/2275_P2) to TG]; Science and Engineering Research Board [EMEQ Award EEQ/2018/000799 to SS].

Notes on contributors

Thorfinnur Gunnlaugsson - School of Chemistry and Trinity Biomedical Sciences Institute, Trinity College Dublin, The University of Dublin, Dublin 2, Ireland; AMBER (Advanced Materials and Bioengineering Research) Centre, Trinity College Dublin, The University of Dublin, Dublin 2, Ireland; orcid.org/0000-0003-4814-6853; E-mail: gunnlaut@tcd.ie

Sankarasekaran Shanmugaraju – Discipline of Chemistry, Indian Institute of Technology Palakkad, Kerala, India; orcid.org/0000-0002-3283-7847; E-mail: shanmugam@iitpkd.ac.in

Author contributions

The manuscript was written through the contributions of all authors. All authors have approved the final version of the manuscript.

References

[1] Cui Y, Yue Y, Qian G, et al. Luminescent functional metal-organic frameworks. Chem Rev. **2012**; 112:1126–1162.

[2] Lustig WP, Mukherjee S, Rudd ND, et al. Metal-organic frameworks: functional luminescent and photonic materials for sensing applications. Chem Soc Rev. **2017**; 46:3242–3285.

[3] Savyasachi AJ, Kotova O, Shanmugaraju S, et al. Supramolecular chemistry: a toolkit for soft functional materials and organic particles. Chem. **2017**; 3:764–811.

[4] Perry Iv JJ, Perman JA, Zaworotko MJ. Design, and synthesis of metal-organic frameworks using metal-organic polyhedra as supermolecular building blocks. Chem Soc Rev. **2009**; 38:1400–1417.

[5] Chen L-J, Yang H-B. Construction of stimuli-responsive functional materials via hierarchical self-assembly involving coordination interactions. Acc Chem Res. **2018**; 51:2699–2710.

[6] Almeida Paz FA, Klinowski J, Vilela SMF, et al. Ligand design for functional metal-organic frameworks. Chem Soc Rev. **2012**; 41:1088–1110.

[7] Lu W, Wei Z, Gu Z-Y, et al. Tuning the structure and function of metal-organic frameworks via linker design. Chem Soc Rev. **2014**; 43:5561–5593.

[8] Chisca D, Croitor L, Petuhov O, et al. Tuning structures and emissive properties in a series of Zn(II) and Cd(II) coordination polymers containing dicarboxylic acids and nicotinamide pillars. CrystEngComm. **2018**; 20:432–447.

[9] Tobin G, Comby S, Zhu N, et al. Towards multifunctional lanthanide-based metal-organic frameworks. Chem Commun. **2015**; 51:13313–13316.

[10] Dolgopolova EA, Rice AM, Martin CR, et al. Photochemistry and photophysics of MOFs: steps towards MOF-based sensing enhancements. Chem Soc Rev. **2018**; 47:4710–4728.

[11] Parmar B, Rachuri Y, Bisht KK, et al. Mechanochemical and conventional synthesis of Zn(II)/Cd(II) luminescent coordination polymers: dual sensing probe for selective detection of chromate anions and TNP in aqueous phase. Inorg Chem. **2017**; 56:2627–2638.

[12] Sorg JR, Wehner T, Matthes PR, et al. Bismuth as a versatile cation for luminescence in coordination polymers from BiX3/4,4′-bipy: understanding of photophysics by quantum chemical calculations and structural parallels to lanthanides. Dalton Trans. **2018**; 47:7669–7681.

[13] Wang L, Wanga W, Xie Z. Tetraphenylethylene-based fluorescent coordination polymers for drug delivery. J Mater Chem B. **2016**; 4:4263–4266.

[14] Allendorf MD, Bauer CA, Bhakta RK, et al. Luminescent metal-organic frameworks. Chem Soc Rev. **2009**; 38:1330–1352.

[15] Liu J-Q, Luo Z-D, Pan Y, et al. Recent developments in luminescent coordination polymers: designing strategies, sensing application and theoretical evidence. Coord Chem Rev. **2020**; 406:213145.

[16] Einkauf JD, Clark JM, Paulive A, et al. A general model of sensitized luminescence in lanthanide-based coordination polymers and metal-organic framework materials. Inorg Chem. **2017**; 56:5544–5552.

[17] Baudron SA. Luminescent metal-organic frameworks based on dipyrromethene metal complexes and BODIPYs. Cryst Eng Comm. **2016**; 18:4671–4680.

[18] Furukawa H, Cordova KE, O'Keeffe M, et al. The chemistry and applications of metal-organic frameworks. Science. **2013**; 341:974.

[19] Cui Y, Li B, He H, et al. Metal-organic frameworks as platforms for functional materials. Acc Chem Res. **2016**; 49:483–493.

[20] Barea E, Montoro C, Navarro JAR. Toxic gas removal - metal-organic frameworks for the capture and degradation of toxic gases and vapours. Chem Soc Rev. **2014**; 43:5419–5430.

[21] Liu D, Lang J-P, Abrahams BF. Highly efficient separation of a solid mixture of naphthalene and anthracene by a reusable porous metal–organic framework through a single-crystal-to-single-crystal transformation. J Am Chem Soc. **2011**; 133:11042–11045.

[22] Liu C-Y, Chen X-R, Chen H-X, et al. Ultrafast luminescent light-up guest detection based on the lock of the host molecular vibration. J Am Chem Soc. **2020**; 142:6690–6697.

[23] Hu F-L, Mi Y, Zhu C, et al. Stereoselective solid-state synthesis of substituted cyclobutanes assisted by pseudorotaxane like MOFs. Angew Chem Int Ed. **2018**; 17:12696–12701.

[24] Gong W-J, Ren Z-G, Li H-X, et al. Cadmium(II) coordination polymers of 4-pyr-poly-2-ene and carboxylates: construction, structure, and photochemical double [2

+ 2] cycloaddition and luminescent sensing of nitroaromatics and mercury(II) ions. Cryst Growth Des. **2017**; 17:870–881.

[25] Sharma A, Istamboulie G, Hayat A, et al. Disposable and portable aptamer functionalized impedimetric sensor for detection of kanamycin residue in milk sample. Sens Actuators B Chem. **2017**; 245:507–515.

[26] Wang B, Lv X-L, Feng D, et al. Highly stable zr(IV)-based metal–organic frameworks for the detection and removal of antibiotics and organic explosives in water. J Am Chem Soc. **2016**; 138:6204–6216.

[27] Zhang -Q-Q, Ying -G-G, Pan C-G, et al. Comprehensive evaluation of antibiotics emission and fate in the river basins of china: source analysis, multimedia modeling, and linkage to bacterial resistance. Environ Sci Technol. **2015**; 49:6772–6782.

[28] Li Y-Z, Wang GD, Lu YK, et al. A multi-functional in(iii)-organic framework for acetylene separation, carbon dioxide utilization, and antibiotic detection in water. Inorg Chem. **2020**; 59:15302–15311.

[29] Shanmugaraju S, Mukherjee PS. π-electron rich small molecule sensors for the recognition of nitroaromatics. Chem Commun. **2015**; 51:16014–16032.

[30] Lin Y, Kong C, Zhang Q, et al. Metal-organic frameworks for carbon dioxide capture and methane storage. Adv Energy Mater. **2017**; 7:1601296–1601324.

[31] Oschatz M, Antonietti M. A search for selectivity to enable CO_2 capture with porous adsorbents. Energy Environ Sci. **2018**; 11:57–70.

[32] Chand S, Pal A, Saha R, et al. Two closely related zn(ii)-mofs for their large difference in co2 uptake capacities and selective co_2 sorption. Inorg Chem. **2020**; 59:7056–7066.

[33] Kumar A, Madden DG, Lusi M, et al. Direct air capture of CO_2 by physisorbent materials. Angew Chem Int Ed. **2015**; 54:14372–14377.

[34] Zhao J, Wang Y-N, Dong WW, et al. A robust luminescent tb(iii)-mof with lewis basic pyridyl sites for the highly sensitive detection of metal ions and small molecules. Inorg Chem. **2016**; 55:3265–3271.

[35] Naskar K, Maity S, Jana S, et al. Arylazoimidazole coordinated and naphthalene-dicarboxylato bridged polymers of co(ii) and photochromic zn(ii) complexes. Cryst Growth Des. **2018**; 18:2986–2997.

[36] Yang X-K, Chen J-D. Crystal-to-crystal transformation and linker exchange in Cd(II) coordination polymers based on flexible bis-pyridyl-bis-amide and 1,4-naphthalenedicarboxylate. CrystEngComm. **2019**; 21:7437–7446.

[37] Karmakar A, Martins LMDRS, Hazra S, et al. Metal-organic frameworks with pyridyl-based isophthalic acid and their catalytic applications in microwave assisted peroxidative oxidation of alcohols and henry reaction. Cryst. Growth Des. 2016;16:1837–1849.

[38] Rúnarsson ÖV, Artacho J, Wärnmark K. The 125th anniversary of the tröger's base molecule: synthesis and applications of tröger's base analogues. Eur J Org Chem. **2012**; 2012:7015–7041.

[39] Samanta PK, English NJ. Triplet harvesting using two-photon absorption in substituted naphthalimides for their application as heavy-atom-free photosensitizers. J Phys Chem C. **2020**; 124 (15):8178–8185.

[40] Zhao Y, Chen K, Yildiz EA, et al. Efficient intersystem crossing in the tröger's base derived from 4-amino-1,8-naphthalimide and application as a potent photodynamic therapy reagent. Chem Eur J. **2020**; 26:3591–3599.

[41] Hawes CS, Fitchett CM, Batten SR, et al. Synthesis and structural characterisation of a Co(II) coordination polymer incorporating a novel dicarboxy-Troger's base/bispyrazole mixed ligand system. Inorg Chem Acta. **2012**; 389: 112–117.

[42] Delente JM, Umadevi D, Shanmugaraju S, et al. Aggregation induced emission (AIE) active 4-amino-1,8-naphthalimide-tröger's base for the selective sensing of chemical explosives in competitive aqueous media. Chem Commun. **2020**; 56:2562–2565.

[43] Shanmugaraju S, Dabadie C, Byrne K, et al. A supramolecular Tröger's base derived coordination zinc polymer for fluorescent sensing of phenolic-nitroaromatic explosives in water. Chem Sci. **2017**; 8:1535–1546.

[44] Shanmugaraju S, McAdams D, Pancotti F, et al. One-pot facile synthesis of 4-amino-1,8-naphthalimide derived tröger's bases via a nucleophilic displacement approach. Org Biomol Chem. **2017**; 15:7321–7329.

[45] Calatrava-Pérez E, Delente JM, Shanmugaraju S, et al. Glycosylated naphthalimides and naphthalimide tröger's bases as fluorescent aggregation probes for con A. Org Biomol Chem. **2019**; 17:2116–2125.

[46] Veale EB, Gunnlaugsson T. Synthesis, photophysical, and dna binding studies of fluorescent tröger's base derived 4-amino-1,8-naphthalimide supramolecular clefts. J Org Chem. **2010**; 75:5513–5525.

[47] Veale EB, Frimannsson DO, Lawler M, et al. 4-amino-1,8-naphthalimide-based tröger's bases as high affinity dna targeting fluorescent supramolecular scaffolds. Org Lett. **2009**; 11:4040–4043.

[48] Banerjee S, Bright SA, Smith JA, et al. Supramolecular approach to enantioselective dna recognition using enantiomerically resolved cationic 4-amino-1,8-naphthalimide-based tröger's bases. J Org Chem. **2014**; 79:9272–9283.

[49] Elmes RBP, Erby M, Bright SA, et al. Photophysical and biological investigation of novel luminescent Ru(II)-polypyridyl-1,8-naphthalimide Tröger's bases as cellular imaging agents. Chem Commun. **2012**; 48:2588–2590.

[50] Shanmugaraju S, Poulsen BLC, Arisa T, et al. Synthesis, structural characterization and antiproliferative activity of a new fluorescent 4-amino-1,8-naphthalimide Troger's base-Ru(II)-curcumin organometallic conjugate. Chem Commun. **2018**; 54:4120–4123.

[51] Shanmugaraju S, Hawes CS, Savyasachi AJ, et al. Supramolecular coordination polymers using a close to 'V-shaped' fluorescent 4-amino-1,8-naphthalimide Tröger's base scaffold. Chem Commun. **2017**; 53:12512–12515.

[52] Banerjee S, Kitchen JA, Bright SA, et al. Synthesis, spectroscopic and biological studies of a fluorescent Pt(II)

(terpy) based 1,8-naphthalimide conjugate as a DNA targeting agent. Chem Commun. **2013**; 49:8522–8524.

[53] Banerjee S, Veale EB, Phelan CM, et al. Recent advances in the development of 1,8-naphthalimide based DNA targeting binders, anticancer and fluorescent cellular imaging agents. Chem Soc Rev. **2013**; 42:1601–1618.

[54] Duke RM, Veale EB, Pfeffer FM, et al. Colorimetric and fluorescent anion sensors: an overview of recent developments in the use of 1,8-naphthalimide-based chemosensors. Chem Soc Rev. **2010**; 39:3936–3953.

[55] Wang H, Wu H, Xue L, et al. A naphthalimide fluorophore with efficient intramolecular PET and ICT Processes: application in molecular logic. Org Biomol Chem. **2011**; 9:5436–5444.

[56] Zheng S, Lynch PLM, Rice TE, et al. Structural effects on the pH-dependent fluorescence of naphthalenic derivatives and consequences for sensing/switching. Photochem Photobiol. **2012**; 11:1675–1681.

[57] Lupo F, Gentile S, Ballistreri FP, et al. Viable route for switching of an engineered silica surface using Cu2+ ions at sub-ppm levels. Analyst. **2010**; 135:2273–2279.

[58] Mitchell KA, Brown RG, Yuan D, et al. A fluorescent sensor for Cu2+ at the sub-ppm level. J Photochem Photobiol, A. **1998**; 115:157–161.

[59] Zhan Y, Zhao J, Yanga P, et al. Multi-stimuli responsive fluorescent behaviors of a donor-π-acceptor phenothiazine modified benzothiazole derivative. RSC Adv. **2016**; 6:92144–92151.

[60] Xue P, Yao B, Wang P, et al. Response of strongly fluorescent carbazole-based benzoxazole derivatives to external force and acidic vapors. RSC Adv. **2014**; 4:58732–58739.

[61] Zhan Y, Yang P, Li G, et al. Reversible piezofluorochromism of a triphenylamine-based benzothiazole derivative with a strong fluorescence response to volatile acid vapors. New J Chem. **2017**; 41:263–270.

[62] Shanmugaraju S, Umadevi D, González Barcia LM, et al. "Turn-on" fluorescence sensing of volatile organic compounds using a 4-amino-1,8-naphthalimide Tröger's base functionalised triazine organic polymer. Chem Commun. **2019**; 55:12140–12143.

[63] Zhao Y, Truhlar DG. The M06 suite of density functionals for main group thermochemistry, thermochemical kinetics, noncovalent interactions, excited states, and transition elements: two new functionals and systematic testing of four M06-class functionals and 12 other functionals. Theor Chem Acc. **2008**; 120:215–241.

[64] Frisch MJ, Trucks GW, Schlegel HB, et al. Gaussian 09, Revision A.1, Wallingford CT: Gaussian, Inc; 2009.

[65] Zhao Y, Wang Y-J, Wang N, et al. Tetraphenylethylene-Decorated Metal–Organic Frameworks as Energy-Transfer Platform for the Detection of Nitro-Antibiotics and White-Light Emission. Inorg Chem. **2019**; 58(19):12700–12706.

[66] Lovitt JI, Hawes CS, Lynes AD, et al. Coordination chemistry of N-picolyl-1,8-naphthalimides: colourful low molecular weight metallo-gelators and unique chelation behaviours. Inorg Chem Frontiers. **2017**; 4: 296–308.

[67] Song Y, Fan R, Du X, et al. Dual functional fluorescent sensor for selectively detecting acetone and Fe^{3+} based on $\{Cu_2N_4\}$ substructure bridged Cu(I) coordination. RSC Adv. **2016**; 6:110182–110189.

[68] Bruker APEX-3, Bruker-AXS Inc., Madison, WI. 2016.

[69] SADABS, Bruker-AXS Inc., Madison, WI. 2016.

[70] Sheldrick GM. SHELXT – Integrated space-group and crystal-structure determination. Acta Crystallogr Sect A. **2015**; 71:3–8.

[71] Sheldrick GM. Crystal structure refinement with SHELXL. Acta Crystallogr. Sect. C. **2015**; 71:3–8.

[72] Spek AL. PLATON SQUEEZE: a tool for the calculation of the disordered solvent contribution to the calculated structure factors. Acta Crystallogr Sect C. **2015**; 71:9–18.

[73] TWINABS, Sheldrick GM 2008, University of Göttingen